Biorheology 00 (2010) 1–16
DOI 10.3233/BIR-2010-0568
IOS Press

A full-range, multi-variable, CFD-based methodology to identify abnormal near-wall hemodynamics in a stented coronary artery

Jonathan B. Murphy * and Fergal J. Boyle
Department of Mechanical Engineering, Dublin Institute of Technology, Dublin, Ireland

Received 30 December 2009
Accepted in revised form 11 June 2010

Abstract. The benefit of coronary stent implantation is reduced by excessive intimal hyperplasia which re-narrows the artery and the prevention of which is still a primary concern for clinicians. Abnormal hemodynamics create non-physiological viscous stress on the artery wall, one of the root causes of intimal hyperplasia following stent implantation. A methodology to comprehensively evaluate the viscous stress on the artery wall following stent implantation would be useful to evaluate a stent's hemodynamic performance.

The proposed methodology employs 3D computational fluid dynamics, the variables wall shear stress (WSS), WSS gradient (WSSG), WSS angle gradient (WSSAG) and a statistical analysis to evaluate the viscous stress. The methodology is demonstrated and compared to a commonly used "threshold technique" for evaluating a stent's hemodynamic performance.

It is demonstrated that the threshold technique is not adequate to fully analyse the viscous stress on the artery wall and can even be misleading. Furthermore, all three of the aforementioned variables should be considered as each provides a different perspective on the abnormalities that can arise in the arterial viscous stress.

The hemodynamic performance of a stent can be assessed more comprehensively than with previously used methods by examining the arterial viscous stresses using the proposed methodology.

Keywords: Stent, intimal hyperplasia, viscous stress, statistical analysis

1. Introduction

Coronary artery disease (CAD) is one of the leading causes of mortality in the developed world. CAD occurs due to the build up of plaque in the coronary arteries which supply blood to the heart muscle. This build up of plaque, a condition known as atherosclerosis, deprives the heart muscle of crucial oxygen and nutrients provided by the coronary blood supply. In the early 1990s bare metal stents (BMSs) were introduced to restore patency to the diseased coronary artery. Basically, a BMS is a metal scaffold inserted into the artery and then, most commonly, expanded by a balloon to relieve the narrowing caused by atherosclerosis. Unfortunately, the stented artery is susceptible to restenosis, defined as a greater than 50% re-blockage of the artery [15]. The prevalence of restenosis with BMSs varies between 10% and 50% depending on the type of stent implanted [18,9,19,28,35]. Restenosis is caused by the excessive growth of new tissue in the stented segment of the artery, a process termed intimal hyperplasia (IH).

* Address for correspondence: J.B. Murphy, Department of Mechanical Engineering, Dublin Institute of Technology, Dublin, Ireland. Tel.: +353 1 402 3963; Fax: +353 1 402 3999; E-mail: jonathan.murphy@dit.ie.

Currently, drug-eluting stents (DESs) are implanted to suppress IH by inhibiting the growth of new tissue. DESs are coated in a drug that is gradually released into the wall of the artery to arrest the proliferation of new tissue cells. The drug coating interrupts the IH process but does not address the factors which initiate the process to begin with.

IH is the arterial response to stent implantation and is stimulated by the injury to the artery wall incurred from the stenting procedure [8,37,38] and by the abnormal near-wall haemodynamics created by the presence of the stent [11,20,21,27,31,34]. Rogers and Edelman [37] demonstrated that arterial injury could be reduced by 42% by altering a stent's geometric configuration while holding stent diameter, mass and surface area the same. This in turn led to a reduction of tissue growth from IH by 38%. Abnormal near-wall haemodynamics affect the viscous stress acting on the artery wall and can influence IH. Sites of low arterial wall shear stress (WSS) with values of less than 0.5 N/m^2 have shown increased IH [21,31]. Sites of increased IH have also been correlated with sites where the WSS gradient (WSSG) exceeds 200 N/m^3 in an end-to-side anastomosis model [34,22] and a rabbit iliac model [27]. These studies demonstrate that arterial injury and abnormal near-wall haemodynamics are two of the underlying stimuli for IH.

Generally, stent haemodynamics are investigated using computational fluid dynamics (CFD) [1–3,6, 5,7,10,13,14,23,39] and the degree of abnormality is often quantified by amounts of arterial surface area below or above certain threshold values of predicted variables. Normalised area with WSS less than 0.5 N/m^2 and with WSSG greater than 200 N/m^3 are the threshold values commonly used to interpret CFD results [1,13,26,24,25,32]. Recently, this "threshold method" identified no significant difference in the abnormal near-wall haemodynamics of four different stents with different *in vivo* restenosis rates [1]. Although the different *in vivo* restenosis rates may be due to the degree of arterial injury and other factors, they may also suggest that the level of detail obtained from the threshold method is not capable of revealing all the IH-inducing abnormal near-wall haemodynamics in the stented artery.

The current work proposes a methodology which provides a detailed analysis of the near-wall haemodynamics in the stented artery. Abnormal near-wall haemodynamics are identified through the prediction of three WSS based variables: WSS, WSSG and wall shear stress angle gradient (WSSAG) [30]. This multi-variable approach improves on previous work by increasing the depth of analysis into the near-wall haemodynamics. The predicted variables are then subject to a statistical analysis to obtain the maximum information from the CFD results. The benefit of this analysis is demonstrated by comparison to the threshold method. The methodology proposed in this paper could be employed to improve the haemodynamic performance of future coronary stents (e.g., BMSs, DESs and bioabsorbable stents) at the design stage by identifying the abnormal near-wall haemodynamics which induce IH.

The paper is laid out as follows: Section 2 describes the methodology employed to predict the three WSS-based variables. The results are presented in Section 3 and finally, the conclusions are presented in Section 4.

2. Materials and methods

2.1. Introduction

A three-dimensional (3D) solid model of the lumen of the stented coronary artery is first generated. This forms the computational domain that is subsequently discretised using an unstructured mesh topology. The governing equations of fluid dynamics are then solved subject to the applied boundary conditions to produce the three Cartesian components of the WSS vector on the arterial surfaces. These

components of the WSS vector are then post-processed to obtain the WSS, WSSG and WSSAG on these surfaces. Histograms of the amount of area contained between specific intervals of the variable values are produced. A statistical analysis is then conducted on the full range of these variables to get the maximum information possible from the predicted results.

This methodology is applied to evaluate the abnormal near-wall haemodynamics resulting from implantation of three different stents in the left anterior descending (LAD) coronary artery. The stents resemble the Palmaz–Schatz (PS) stent (Johnson and Johnson Interventional System, Warren, NJ, USA), the Gianturco–Roubin II (GR-II) stent (Cook Inc., Bloomington, IN, USA) and the Cordis Bx-Velocity (Bx) stent (Johnson and Johnson Interventional System, Warren, NJ, USA). These contrasting stent designs are chosen to investigate if the notable differences in their geometries produce significantly different haemodynamic disturbances in the artery. Also, the prior knowledge of the *in vivo* performance of these stents is useful when analysing the results as abnormal near-wall haemodynamics may have contributed to their restenosis rates. The PS stent consists of two 7 mm long slotted-tube sections joined by a central articulation and is commonly used in computational modelling due to its generic design. In one clinical trial, the PS stent had a restenosis rate of 20.6% [28]. The GR-II stent on the other hand performed poorly in the same trial with a restenosis rate of 47.3% [28]. The GR-II stent has a coil design consisting of widely-spaced interdigitating loops. The Bx stent is of a closed cell design with thick struts connected by S-shaped connectors. Implantation of the Bx stent resulted in a restenosis rate of 31.4% in the ISAR-STERO II trial [35].

2.2. Computational fluid dynamics

2.2.1. Computational domain

The 3D solid model is created beginning with a solid cylinder measuring the length and external diameter of the stent; this is the region of interest with details provided in Table 1. The geometry of the stent is then removed from the cylinder. The solid model is extended proximal and distal to the stented section by adding cylinders 21.3 mm long, which equals to the entrance length for fully-developed laminar flow. These cylinders have diameters of 3.2 mm which creates a stent-to-artery deployment ratio of 1.09:1 similar to a normal *in vivo* value [28]. These extra lengths ensure the region of interest is not affected by the inlet and outlet boundary flow conditions. A tapered section of 2 mm in length connects the stented and unstented sections similar to a previous numerical study [24].

A sensitivity analysis was performed to investigate the effect of taper length on the WSS in the region of interest. The mean WSS in a 14.3 mm long section of a 3.5 mm diameter artery was 0.797, 0.804 and 0.809 N/m when the taper lengths were 1.5, 2.0 and 2.5 mm, respectively, and the smaller diameter was

Table 1
Geometric characteristics of the stent models. Certain values are normalised by the stent length

Stent	Palmaz–Schatz	Gianturco–Roubin II	Bx-Velocity
Length (mm)	14.30	20.00	12.50
Internal diameter (mm)	3.5	3.5	3.5
Strut dimensions (mm)	0.0635×0.152	0.076×0.172	0.14×0.13
Stent surface area (mm^2)	108.92	83.84	100.31
Prolapsing tissue volume (mm^3)	5.71	15.12	6.52
Normalised prolapsing tissue volume (mm^3/mm)	0.40	0.76	0.52
Stent/tissue contact area (mm^2)	44.71	30.91	23.69
Normalised stent tissue contact area (mm^2/mm)	3.13	1.55	1.90

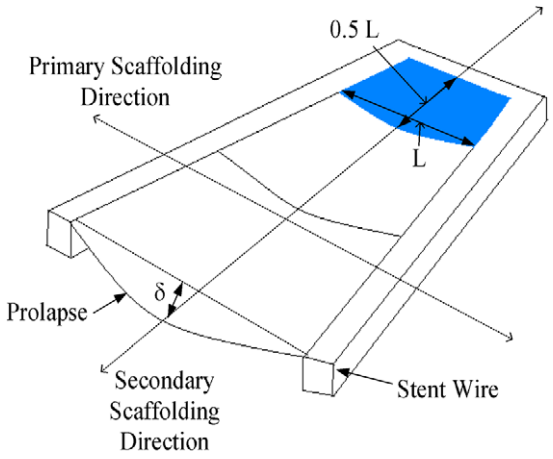

Fig. 1. Illustration of the primary and secondary scaffolding direction of part of the PS stent. The arterial tissue protrudes a depth δ into the stented artery and is supported in the primary scaffolding direction and partially supported (shaded section) in the secondary scaffolding direction.

3.2 mm. Therefore, either increasing or decreasing the taper length by 0.5 mm, resulted in less than a 1% change in mean WSS in the region of interest.

In the geometric model, the assumption is made that the stenotic plaque has been completely compressed against the wall. Then, a novel methodology to numerically predict tissue prolapse between stent struts [32] is employed. Briefly, the prolapsing tissue creates a variable artery radius r given by

$$\frac{r}{R_o} = 1 - \frac{x\delta}{2R_o}\left\{1 + \cos\frac{2\pi}{L}\left(z - \frac{L}{2}\right)\right\}, \tag{1}$$

where R_o is the external diameter of the stent, L is the distance between the stent struts in the primary scaffolding direction and δ is the prolapse depth equal to the product of L and a constant C obtained from finite element analysis data [36]. The variable x is a prolapse reduction factor initiated at a distance of $0.5L$ from struts offering secondary scaffolding support as shown in Fig. 1.

This prolapsing tissue is then removed from the solid model. The solid models of the stented region of interest and the tapered section are shown in Fig. 2. The geometric characteristics given in Table 1 detail some of the major scaffolding features of each stent model.

2.2.2. *Computational mesh*

The computational domains are discretised using an unstructured mesh topology. This is achieved in ANSYS Workbench 12.0 using the advancing front method. A mesh convergence study is conducted for all stents to ensure the results are independent of the computational mesh density. Results are considered mesh converged when the difference in the RMS values of the WSS and WSSG between successive mesh densities is less than 4% along a sample line similar to a strategy employed in a previous numerical study [23]. Mesh convergence is achieved with 4,551,484 elements for the PS stent, 3,038,536 elements for the GR-II stent and 5,840,890 elements for the Bx stent. Results from the mesh convergence study are shown in Fig. 3 for the GR-II stent.

2.2.3. *Governing flow equations*

The flow in the stented artery is assumed steady, laminar and incompressible. In this work, a transient analysis is not deemed necessary to demonstrate the advantage of the current methodology. To predict

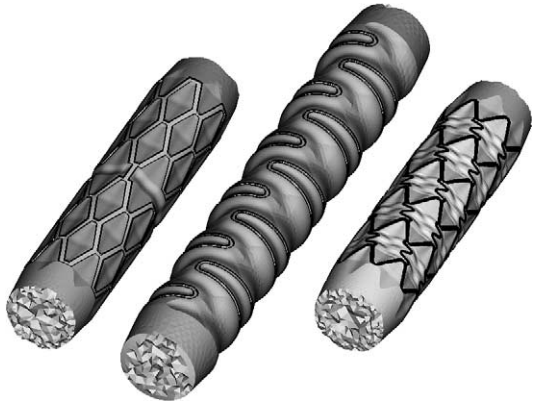

Fig. 2. Solid models of the LAD arteries implanted with the PS stent (left), the GR-II stent (middle) and the Bx stent (right).

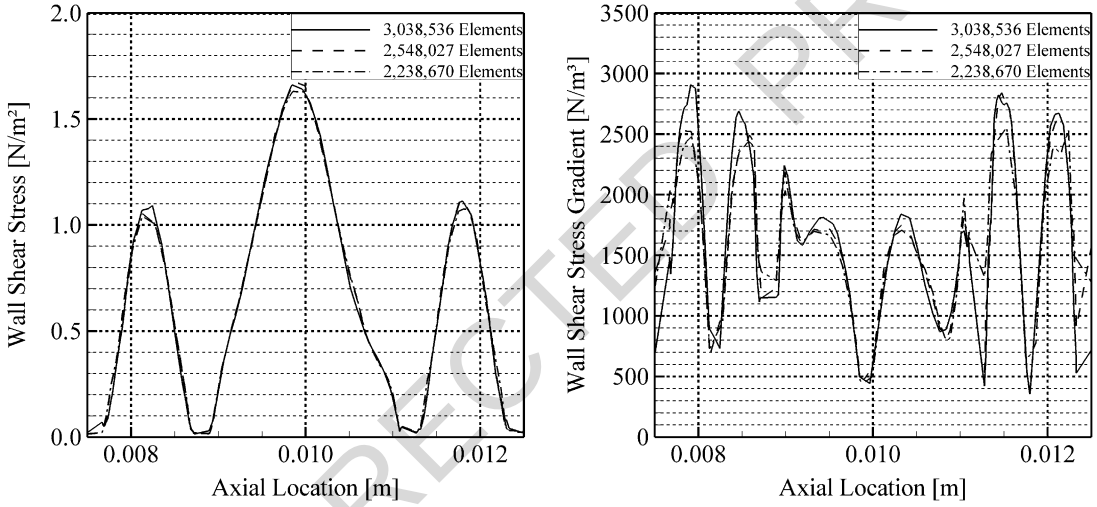

Fig. 3. Magnitude of WSS and WSSG along a sample axial line which crosses two struts of the GR-II stent for three mesh densities.

the flow the CFD code solves the general form of the conservation of mass and momentum equations which are given in vector form in Eqs (2) and (3), respectively

$$\frac{\partial \rho}{\partial t} + \vec{\nabla} \cdot (\rho \vec{V}) = 0, \tag{2}$$

$$\frac{\partial \rho \vec{V}}{\partial t} + \vec{\nabla} \cdot (\rho \vec{V} \otimes \vec{V}) = -\vec{\nabla} p + \vec{\nabla} \cdot (\vec{\vec{\tau}}_{ij}), \tag{3}$$

where ρ is the fluid density, p is the static pressure, $\vec{V}$ is the velocity vector, μ is the fluid dynamic viscosity and $\vec{\vec{\tau}}_{ij}$ is the shear stress tensor written

$$\vec{\vec{\tau}}_{ij} = \mu(\vec{\nabla}\vec{V} + \vec{\nabla}\vec{V}^{\mathrm{T}}). \tag{4}$$

At low shear rates (0–100 s^{-1}) blood exhibits the non-Newtonian behaviour of variable fluid dynamic viscosity which is dependant on the shear rate. This non-Newtonian nature of the flow is accommodated using the Carreau model [17] written

$$\mu = \mu_\infty + (\mu_0 - \mu_\infty)[1 + (\gamma\lambda)^2]^{((q-1)/2)}, \tag{5}$$

where γ is the shear rate calculated as the second invariant of the strain-rate tensor and the constants are

$$\begin{aligned} &\mu_0 = 0.056\ \mathrm{N \cdot s \cdot m^{-2}}, \qquad \lambda = 3.31\ \mathrm{s}, \\ &\mu_\infty = 0.00345\ \mathrm{N \cdot s \cdot m^{-2}}, \qquad q = 0.375. \end{aligned} \tag{6}$$

The commercial software code ANSYS CFX Version 12 (Canonsburg, PA, USA) is used to solve the governing equations in the computational domain using a vertex-centred finite volume scheme which is second order accurate in space.

2.2.4. Boundary conditions

Boundary conditions must be applied at all exterior boundaries of the computational domain to define the flow. A fully-developed, laminar, axial-velocity-profile is applied at the inlet given by

$$\vec{V} = \vec{V}_{\mathrm{Max}}\left(1 - \frac{r^2}{R_\mathrm{o}^2}\right), \tag{7}$$

where the variable r is the radial coordinate measured from the centreline and R_o is the wall radius of 1.6 mm. $\vec{V}_{\mathrm{Max}}$ is the maximum centreline velocity given a value which corresponds to a blood volume flow rate of 55 ml/min. This corresponds to the mean flow rate in the human LAD coronary artery under resting conditions [33]. The decision to use these mean flow properties is based on the desire to predict constant typical values of the WSS acting in the stented artery. A fixed static pressure of zero N/m^2 is applied at the outlet of the domain. The no-slip boundary condition is applied on all surfaces representative of the artery wall and the stent struts.

2.2.5. Solution strategy

The CFD code uses a coupled solver, solving the governing flow equations as a single system at each timestep. This solution approach uses a fully implicit discretisation of the equations at any given timestep. The timestep behaves like an 'acceleration parameter', to guide the approximate solutions in a physically based manner to a steady-state solution. The convergence criterion for the maximum velocity and density residuals is set at 10^{-5}. The discretised equations are solved using parallel processing with a MeTiS multilevel weighted k-way partitioning algorithm. The computations are conducted on a HP xw6400 64-bit workstation with a quad Intel (Xeon) 2 GHz processor with 6 GB of RAM and 80 GB hard disk space.

2.3. Post-processing

2.3.1. Introduction

The post-processing of the predicted WSS vectors, conducted in Tecplot 360 2008 (Bellevue, WA, USA), produces the magnitudes of the WSS, WSSG and WSSAG on the arterial surfaces. The methodology employed to calculate the distribution of these variables is described below along with a description of the statistical analysis.

2.3.2. Wall shear stress

The dot product of the unit normal vector of a surface denoted $\vec{l}$ and the viscous stress tensor denoted $\vec{\tau}_{ij}$ yields the WSS vector and in Cartesian coordinates is written

$$\vec{l} \cdot \vec{\tau}_{ij} = \vec{\tau}_{w_{xyz}} = \tau_{w,x}\vec{i} + \tau_{w,y}\vec{j} + \tau_{w,z}\vec{k}. \tag{8}$$

The magnitude of the WSS vector is equal to the viscous shear stress acting on the surface and calculated as

$$WSS = (\tau_{w,x}^2 + \tau_{w,y}^2 + \tau_{w,z}^2)^{1/2}. \tag{9}$$

Physiologic arterial $WSS > 1.5$ N/m^2 has been shown to promote endothelial quiescence in the artery [31] and to reduce IH [4]. Numerous studies have shown positive correlation between IH and sites with lower than normal physiologic WSS values [11,21,27,40,41].

2.3.3. Wall shear stress gradient

The WSSG is a measure of the spatial rate of change of the magnitude of the WSS vector. The WSSG is obtained by first calculating the gradient of the WSS vector in Cartesian coordinates, which results in a nine component tensor. In order to calculate the magnitude of the WSSG acting on the artery surface, the WSSG tensor must be transformed from the Cartesian coordinate system to a local coordinate system by a standard component-wise tensor transformation explained in detail elsewhere [20]. The three mutually-orthogonal axes of a local coordinate system are taken as m, the WSS direction, n, tangential to the surface and normal to m, and l, the surface normal direction. The components of the local WSSG tensor that act tangentially to the surface are then

$$\vec{\nabla}\vec{\tau}_{w_{mnl}} = \begin{pmatrix} \frac{\partial \tau_{w,m}}{\partial m} & \frac{\partial \tau_{w,m}}{\partial n} \\ \frac{\partial \tau_{w,n}}{\partial m} & \frac{\partial \tau_{w,n}}{\partial n} \end{pmatrix}. \tag{10}$$

The diagonal components $\partial\tau_{w,m}/\partial m$ and $\partial\tau_{w,n}/\partial n$ create tension between adjacent endothelial cells which line the artery. This causes widening and shrinking of the cellular gaps. The components $\partial\tau_{w,m}/\partial n$ and $\partial\tau_{w,n}/\partial m$ cause relative movement of adjacent cells. Lei et al. [29] suggest that the components causing the intracellular tension are the most important with respect to IH and, with this in mind, the magnitude of the WSSG is calculated as

$$WSSG = \left[\left(\frac{\partial \tau_{w,m}}{\partial m}\right)^2 + \left(\frac{\partial \tau_{w,n}}{\partial n}\right)^2\right]^{1/2}. \tag{11}$$

2.3.4. Wall shear stress angle gradient

The directional changes in the WSS vector, not accounted for in the WSSG calculation, may also lead to IH [30]. A mesh independent WSS directional parameter is formulated by using the gradient operator. Using the WSS vector at the node of interest as a reference, angular differences given by

$$\phi = \pm\cos^{-1}\left(\frac{\vec{\tau}_o \times \vec{\tau}_r}{|\vec{\tau}_o| \times |\vec{\tau}_r|}\right), \qquad -180 < \phi \leqslant 180, \tag{12}$$

are assigned to the neighbouring nodes where $\vec{\tau}_o$ is the WSS vector at the node of interest and $\vec{\tau}_r$ is the WSS vector at the neighbour node. Taking the spatial gradient of these angular differences at the node of interest yields the wall shear stress angle gradient (WSSAG) vector written

$$\overrightarrow{WSSAG} = \frac{\partial \phi}{\partial x}\vec{i} + \frac{\partial \phi}{\partial y}\vec{j} + \frac{\partial \phi}{\partial z}\vec{k}. \tag{13}$$

The magnitude of the WSSAG is calculated as

$$WSSAG = \left(\left(\frac{\partial \phi}{\partial x}\right)^2 + \left(\frac{\partial \phi}{\partial y}\right)^2 + \left(\frac{\partial \phi}{\partial z}\right)^2\right)^{1/2} \tag{14}$$

and is the maximum rate of change of WSS angle with respect to unit space. Endothelial cells have been shown to align themselves in the WSS direction [31], and the WSSAG can therefore be used to identify sites where gaps may be produced between endothelial cells which may lead to IH.

2.3.5. Statistical analysis

As the CFD solver employs a vertex-centred finite volume scheme, the WSS, WSSG and WSSAG are computed at the vertices of the surface faces. Face-averaged values of these variables are then calculated for each face as

$$\phi_j = \frac{\sum_{i=1}^{n} \phi_i}{n} \tag{15}$$

where ϕ is the variable, j is the face number and the summation is over the n vertices attached to the face j. The area distribution of each face-averaged variable is visualised using histograms by displaying the amount of area contained between specific intervals of the variable value. In addition to this qualitative technique, the area-weighted mean, standard deviation and kurtosis of the distribution of each variable are also calculated for quantitative analysis.

The area-weighted mean represents the average value of the variable in the stented region of the artery. The standard deviation provides a measure of the typical difference between variable values and the mean value. A high standard deviation signifies the existence of areas where the variable value may be much higher or lower than the mean. The kurtosis provides an extra measure of the variable value deviations from the mean in the distribution and is equal to the average of the tesseracts of the deviations normalised by the tesseract of the standard deviation. A high kurtosis can therefore signify that the value of the standard deviation is being driven upwards by a small number of data points where the deviation is very high. The lowest kurtosis value possible is 1. This would happen if all variable values were at one standard deviation from the mean. In general, the kurtosis quantifies the influence of data points with very high deviations on the standard deviation.

3. Results

3.1. Introduction

CFD results are presented for the models of the LAD artery implanted separately with the three different stents. The next three subsections contain the results for the calculated WSS, WSSG and WSSAG

variables, respectively. The results are displayed in histogram form for each variable. The histograms display the amount of arterial tissue area contained between specific intervals of each face-averaged variable. The area in the histograms is normalised by the total area analysed, which is the tissue area confined within the axial limits of the stent. Greyscale contour plots are also provided to help visualise the predicted variables on the artery wall. The distribution of the three variables is quantified by the statistical analysis given with the histograms.

3.2. Wall shear stress

The WSS results are presented in Figs 4 and 5. The WSS for the fully-developed flow near the inlet of the unstented section is constant with a value of 1.21 N/m^2 for all stents. The statistical analysis of the distribution of WSS shown in Fig. 4 reveals that the mean WSS is similar for the PS and GR-II stents with values of 0.753 and 0.757 N/m^2, respectively. The Bx stent has a significantly lower mean value of 0.516 N/m^2. Figure 5 shows large amounts of area around the Bx stent struts where the WSS is low ($<$0.5 N/m^2) which explains this comparatively lower mean value.

The standard deviation is approximately 32% higher for the GR-II stent compared to the PS and Bx stents. This highlights the wider distribution of arterial WSS values visible in Fig. 4. This is due to the high WSS values at the peaks of the prolapse and lower values in the troughs around the GR-II stent struts shown in Fig. 5. Data in Table 1 shows that the GR-II stent allows more tissue to prolapse into the artery than the other stents. The higher standard deviation quantifies a haemodynamic effect of the larger volume of prolapsing tissue with the GR-II stent.

The kurtosis is 60% and 66% higher for the PS stent compared to the GR-II and Bx stents, respectively, indicating the standard deviation value is influenced more so by small arterial tissue areas where the value of the WSS deviates greatly from the mean. Figure 5 shows these areas of tissue at the peaks of the prolapsing tissue at the articulation site. The thinner struts of the PS stent have lead to a more uniform distribution of WSS in each of the closed cells in comparison to the wider spread of values in the closed

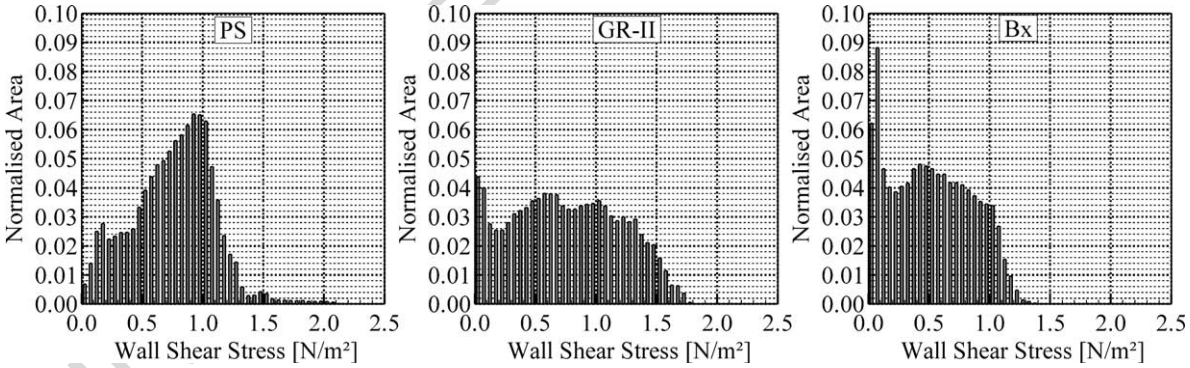

Stent	Mean (N/m²)	Standard Deviation (N/m²)	Kurtosis
Palmaz–Schatz	0.753	0.337	3.189
Gianturco–RoubinII	0.757	0.445	1.995
Bx-Velocity	0.516	0.334	1.916

Fig. 4. Distribution and statistical analysis of the WSS. The bars represent the amount of normalised area with WSS values bounded by the tick marks on the abscissa.

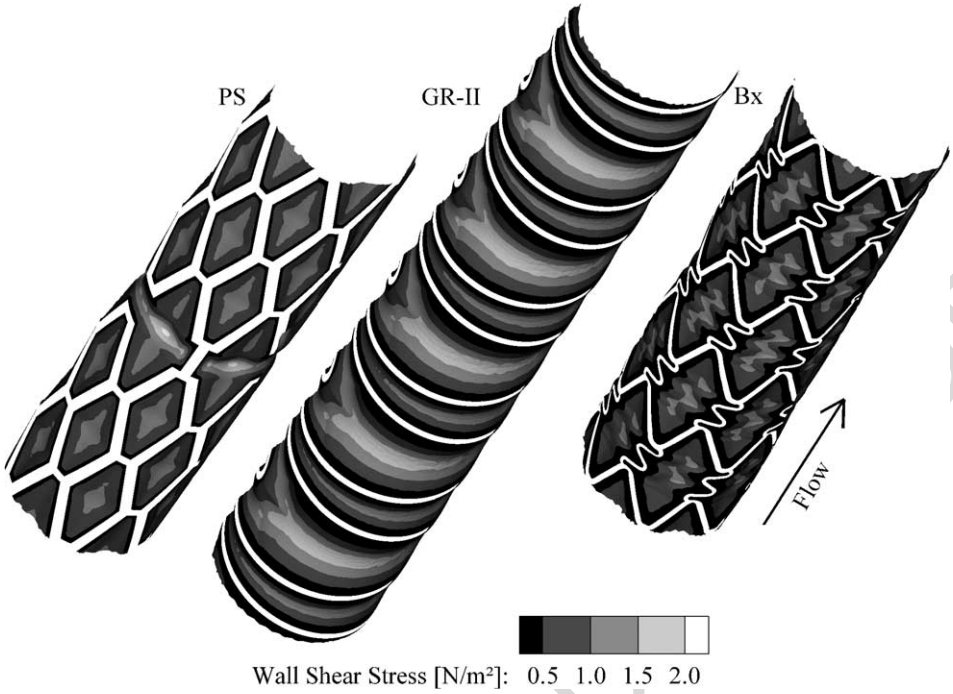

Fig. 5. Contour plots of the WSS on the arterial tissue in the stented arteries.

cells of the Bx stent. This haemodynamic effect which is attributable to the contrasting stent geometries is captured by the different kurtosis values for the PS and Bx stents.

Since low WSS encourages IH, the Bx stent performs poorly compared to the PS and GR-II stents, creating large areas of low WSS around its struts that only briefly recover to values above 1 N/m^2 in the cell centres. The mean WSS values are similar, but the analysis uncovers the distinction between the PS and GR-II stents. The PS stent has a reasonably uniform WSS distribution over the majority of the stented region with small high-deviation regions at the articulation and very close to the struts. In contrast the GR-II stent has larger areas of low WSS near the struts which spatially change quickly to high values.

The threshold method of comparison shows 22.8%, 32.2% and 50.0% of the stented region exposed to WSS in the range of 0.0–0.5 N/m^2 for the PS, GR-II and Bx stents, respectively. The threshold method therefore favours the PS stent followed by the GR-II and then Bx stent, which is in agreement with the analysis above. However, the threshold method does not identify the complex stent-design-related distribution of WSS on the artery wall.

3.3. Wall shear stress gradient

Figures 6 and 7 contain the results for the WSSG. The mean value for the GR-II stent is 74% higher than that for the PS stent and 55% higher than that for the Bx stent. The GR-II stent struts which traverse the flow create proximal and distal areas of low WSS. The WSS value then quickly increases in the axial direction as discussed in Section 3.2. This creates the large WSSGs between the struts which are visible

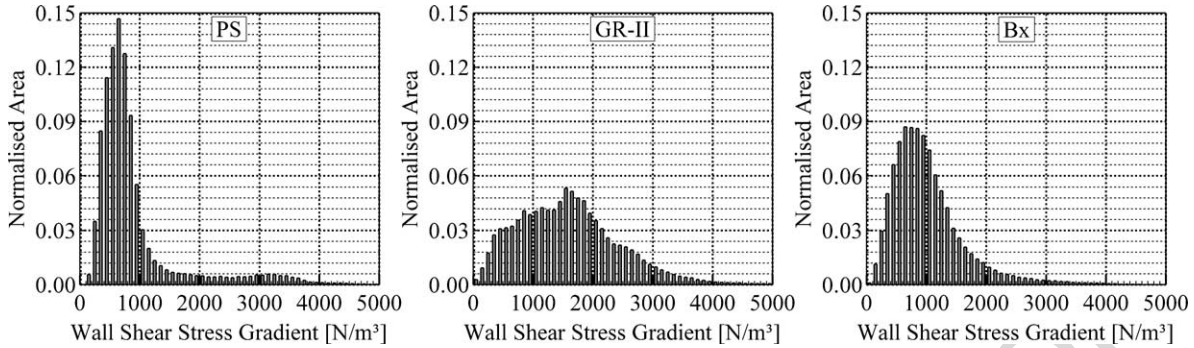

Stent	Mean (N/m³)	Standard Deviation (N/m³)	Kurtosis
Palmaz–Schatz	920.6	770.3	9.1
Gianturco–RoubinII	1599.5	858.8	3.9
Bx-Velocity	1028.8	621.2	8.0

Fig. 6. Distribution and statistical analysis of the WSSG. The bars represent the amount of normalised area with WSSG values bounded by the tick marks on the abscissa.

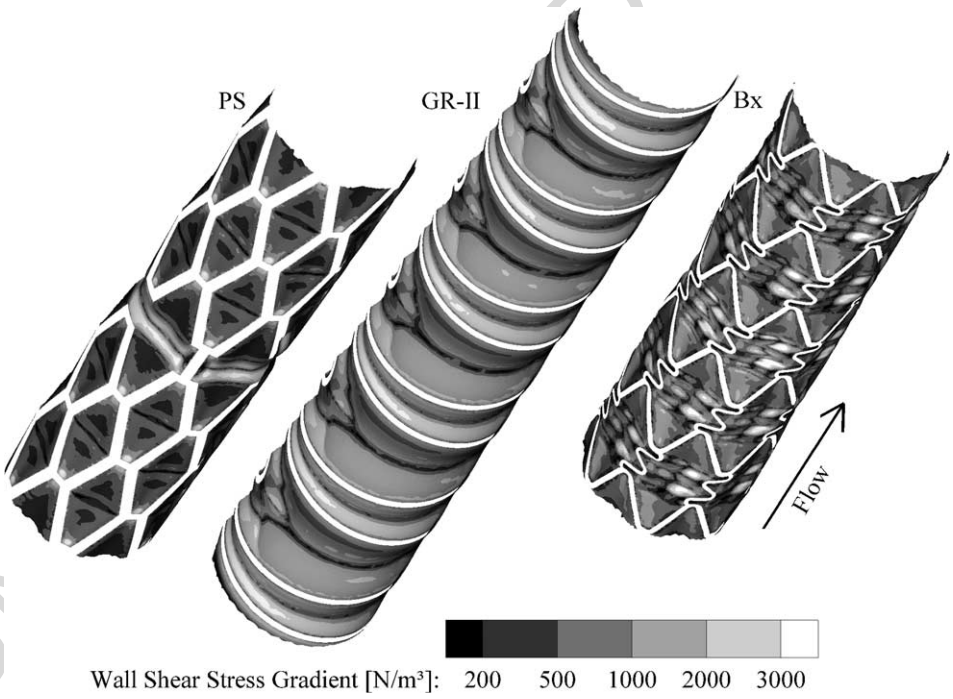

Fig. 7. Contour plots of the WSSG on the arterial tissue in the stented arteries.

in Fig. 7 and are quantified by the large mean value. The mean WSSG value for the Bx stent is 12% higher than that for the PS stent. Figure 7 shows regions of $WSSG > 2000$ N/m^3 on the uneven prolapse near the S-connectors of the Bx stent which contribute to this higher value.

The standard deviation of the WSSG for the GR-II stent is 858.8 N/m^3, 12% and 38% higher than the PS and Bx stents, respectively. This signifies large spatial fluctuations in the WSSG acting on the arterial tissue. Figure 7 illustrates this effect, with large regions of high WSSG (>3000 N/m^3) on the proximal side of the smallest inter-strut regions and low WSSG (<200 N/m^3) in the middle of the largest inter-strut regions of the GR-II stent. The standard deviation is 24% higher for the PS stent when compared to the Bx stent. However, the higher kurtosis value for the PS stent indicates that the standard deviation is influenced by small areas of tissue with very high WSSG values (>3000 N/m^3). In contrast the Bx stent has larger areas with high WSSG values of 1000–2000 N/m^3 as shown in the histogram in Fig. 6 and the contour plot in Fig. 7. This demonstrates how the histograms, statistical measures and contour plots compliment each other to reveal the detail of the variable distributions produced by the different stent designs.

The large WSSGs produced in the inter-strut regions of the GR-II stent have implicated it as the worst performing stent with regard to this variable. Comparing Bx and PS stents, the higher mean and lower kurtosis values place the Bx stent second, with the PS again performing the best. Using thresholds, the PS stent has 0.6% of its stented region with $WSSG < 200$ N/m^3 compared to 1.2% for the GR-II and Bx stents. This negligible amount of tissue below the threshold value is insufficient to distinguish between the stents. This is a clear demonstration of the weakness of the threshold method to fully analyse the predicted variable on the artery wall.

3.4. Wall shear stress angle gradient

To the authors' knowledge no upper threshold has ever been defined in the literature for the WSSAG, such that an artery with WSSAG values above this threshold can be considered to be at an elevated risk for IH. Indeed, the authors' consider this to be the first time this variable has been predicted in a model of a stented artery. The performance of the stents with regard to this variable can easily be evaluated using the analysis technique applied for the other variables.

The results for the WSSAG are presented in Figs 8 and 9. A semi-logarithmic scale is used on the histogram in Fig. 8 to accommodate the large range of this variable. The mean WSSAG value for the GR-II stent is 33.4 rad/mm, 163% higher than that for the PS stent and 42% higher than that for the Bx stent. The flow traversing struts of the GR-II stent have created large areas of separation and reattachment proximal and distal to the struts creating very high WSSAG values (>100 rad/mm). These regions of high WSSAG are also visible around the S-connectors of the Bx stent as shown in Fig. 9. These effects are quantifiable from the comparison of the mean values.

The standard deviation is the highest for the GR-II stent, 79% higher than the PS stent and 88% higher than the Bx stent. Figure 9 shows large areas of low WSSAG (<5 rad/mm) between the large inter-strut regions. This effect coupled with the very high WSSAG near the GR-II struts discussed above is highlighted by the high standard deviation value.

The standard deviations are similar for the PS and Bx stents. However, the kurtosis provides an extra measure of contrast of the WSSAG distribution between the two stents. The higher kurtosis for the PS stent signifies small areas of tissue under very high WSSAG values (>100 rad/mm) influencing the standard deviation, whereas the lower kurtosis for the Bx stent signifies larger amounts of tissue in the high range of WSSAG (20–100 rad/mm). This distribution is displayed in the histogram in Fig. 8.

The analysis shows that the GR-II stent is the worst stent with more area under the high WSSAG values. This is followed by the Bx stent and finally the PS stent which performs the best. The high kurtosis values with this variable compared to other variables reflects that the WSSAG is generally low in the stented region but has high magnitudes in regions of highly disturbed flow.

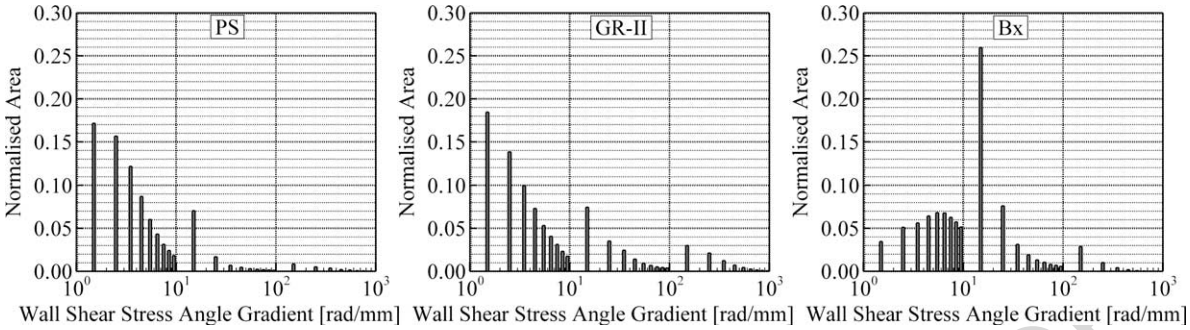

Stent	Mean (rad/mm)	Standard Deviation (rad/mm)	Kurtosis
Palmaz–Schatz	12.7	56.5	124.9
Gianturco–RoubinII	33.4	101.4	41.2
Bx-Velocity	23.6	53.8	83.6

Fig. 8. Distribution and statistical analysis of the WSSAG. The bars represent the amount of normalised area with WSSAG values bounded by the tick marks on the abscissa.

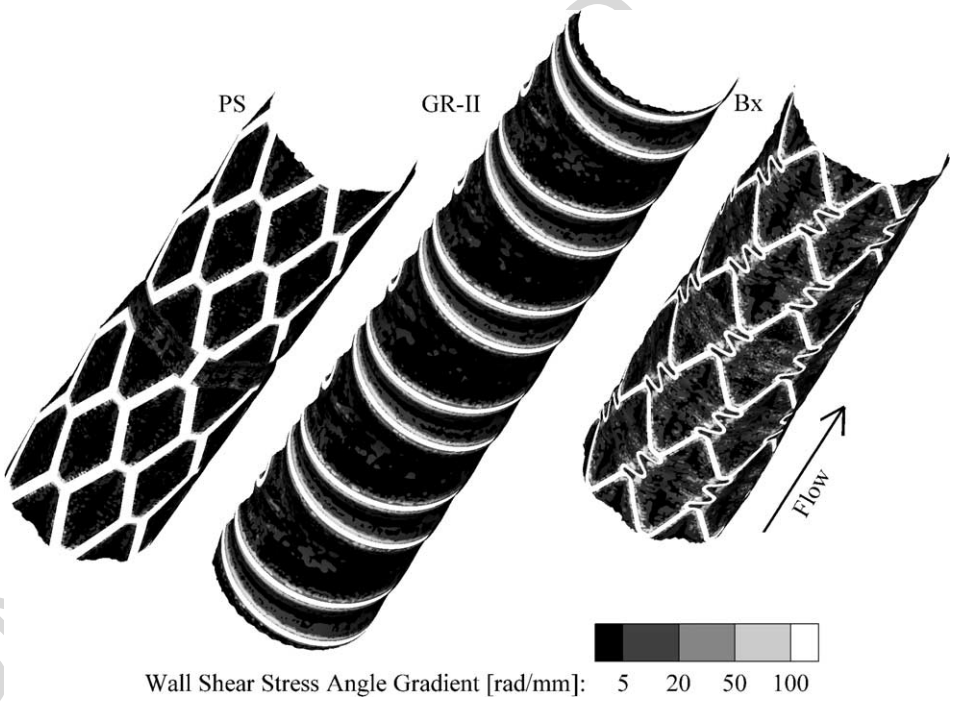

Fig. 9. Contour plots of the WSSAG on the arterial tissue in the stented arteries.

4. Conclusion

In this work a methodology is presented to assess a stent based on the near-wall haemodynamics in the stented artery. A CFD analysis is conducted to predict the WSS vectors acting on the arterial tissue in the

stented artery. The components of the WSS vectors are then post-processed to calculate the magnitude of the predicted WSS, WSSG and WSSAG. A statistical analysis is then conducted to obtain the maximum information from the variables.

Both the proposed analysis technique and the threshold method identify the Bx as being the less attractive of the stents with regard to WSS. However, using the histograms as a visual aid and quantifying the results using the statistical analysis much more information is revealed about the distribution of the variable. Examination of the WSSG variable reveals a weakness in the threshold method of stent assessment. The threshold method only slightly distinguishes between the stents. The statistical analysis of the WSSG clearly demonstrates that the GR-II is the poorest performing stent with regard to this variable. This is a prime example of the benefit of the proposed methodology. There is no threshold method comparison to be made for the WSSAG, as no threshold has been defined in the literature. The statistical analysis has once again proved its robustness in easily identifying how the features of the stent influence the distribution of this variable in the stented artery. The GR-II stent is again the poorest performing stent.

Each of the variables employed in this methodology highlights the different adverse haemodynamic features which could lead to IH development. If stent performance were based solely on WSS as is sometimes the case [1], the Bx would be implicated as the worst stent. However, the multi-variable approach employed in this work seems to favour the stents in the order of PS, Bx and GR-II. This also correlates with the order of stent restenosis rates indicating that adverse haemodynamics may be partly responsible for the *in vivo* performance of these stents. This methodology is applicable to BMSs, DESs and any future stents that alter the haemodynamics of the artery after implantation. The results identify one of the key stimuli for IH in the implanted artery and as such are important for all types of stent.

Limitations include the assumptions of fully-developed, steady, laminar flow, a rigid stent and arterial wall and an idealised model of prolapsing tissue. Since actual tissue prolapse *in vivo* is likely be patient specific, an option to omit the idealised prolapse model in order to investigate the effect of the stent geometry alone could be considered. However, the shape of the prolapsing tissue is determined by the stent geometry and as such, is in itself a feature of the stent. Since tissue prolapse is known to occur *in vivo* [16], the inclusion of the idealised prolapse model should produce more realistic results. In the analysis of the results, the kurtosis is used to indicate the existence of small areas exposed to highly abnormal variable values. With regard to stent performance, the assumption is made that large areas of moderately abnormal variable values are worse than small areas of highly abnormal variable values. This assumption is based on the fact that tissue growth generally occurs where necessary to restore the variables back to normal values [27,12]. It is likely that the large areas with moderately abnormal variable values would require a greater volume of tissue growth to be restored back to normal values, and are therefore more likely to result in restenosis.

The main objective of this work is to introduce a more complete method of post-processing and analysing results obtained from a simulation performed on physiologically realistic models of the stented artery. The methodology presented here provides a novel, accurate, and efficient way to assess and compare different stents based on the haemodynamic WSS-based variables and this should assist in stent design in the future.

References

[1] R. Balossino, F. Gervaso, F. Migliavacca et al., Effects of different stent designs on local hemodynamics in stented arteries, *J. Biomech.* **41** (2008), 1053–1061.

[2] R.K. Banerjee, S.B. Devarakonda, D. Rajamohan et al., Developed pulsatile flow in a deployed coronary stent, *Biorheology* **44** (2007), 91–102.
[3] J. Berry, A. Santamarina, J.E. Moore Jr. et al., Experimental and computational flow evaluation of coronary stents, *Ann. Biomed. Eng.* **28** (2000), 386–398.
[4] S.G. Carlier, L.C.A. van Damme, C.P. Blommerde et al., Augmentation of wall shear stress inhibits neointimal hyperplasia after stent implantation: inhibition through reduction of inflammation?, *Circulation* **107** (2003), 2741–2746.
[5] N. Duraiswamy, R.T. Schoephoerster and J.E. Moore Jr., Comparison of near-wall hemodynamic parameters in stented artery models, *J. Biomech. Eng.* **131** (2009), 061006.
[6] N. Duraiswamy, J.M. Cesar, R.T. Schoephoerster et al., Effects of stent geometry on local flow dynamics and resulting platelet deposition in an *in vitro* model, *Biorheology* **45** (2008), 547–561.
[7] N. Duraiswamy, R.T. Schoephoerster, M.R. Moreno et al., Stented artery flow patterns and their effects on the artery wall, *Annu. Rev. Fluid Mech.* **39** (2007), 357–382.
[8] E.R. Edelman and C. Rogers, Pathobiologic responses to stenting, *Am. J. Cardiol.* **81** (1998), 4E–6E.
[9] J. Escaned, J. Goicolea, F. Alfonso et al., Propensity and mechanisms of restenosis in different coronary stent designs: Complementary value of the analysis of the luminal gain–loss relationship, *J. Am. Coll. Cardiol.* **34** (1999), 1490–1497.
[10] A.O. Frank, P.W. Walsh and J.E. Moore Jr., Computational fluid dynamics and stent design, *Artif. Organs* **26** (2002), 614–621.
[11] M.H. Friedman, G.M. Hutchins, C.B. Bargeron et al., Correlation between intimal thickness and fluid shear in human arteries, *Atherosclerosis* **39** (1981), 425–436.
[12] J.M. Garasic, E.R. Edelman, J.C. Squire et al., Stent and artery geometry determine intimal thickening independent of arterial injury, *Circulation* **101** (2000), 812–818.
[13] Y. He, N. Duraiswamy, A.O. Frank et al., Blood flow in stented arteries: a parametric comparison of strut design patterns in three dimensions, *J. Biomech. Eng.* **127** (2005), 637–647.
[14] F.S. Henry, Flow in stented arteries, in: *Intra- and Extracorporeal Cardiovascular Fluid Dynamics*, P. Verdonck and K. Perktold, eds, WIT Press, Boston, 2003, pp. 333–364.
[15] D.R. Holmes Jr., R.E. Vlietstra, H.C. Smith et al., Restenosis after percutaneous transluminal coronary angioplasty (PTCA): a report from the PTCA Registry of the National Heart, Lung, and Blood Institute, *Am. J. Cardiol.* **53** (1984), 77C–81C.
[16] I. Jang, G. Tearney and B. Bouma, Visualization of tissue prolapse between coronary stent struts by optical coherence tomography: comparison with intravascular ultrasound, *Circulation* **104** (2001), 2754.
[17] H. Jung, J.W. Choi and C.G. Park, Asymmetric flows of non-Newtonian fluids in a symmetric stenosed artery, *Korea–Aust. Rheol. J.* **16** (2004), 101–108.
[18] A. Kastrati, J. Mehilli, J. Dirschinger et al., Restenosis after coronary placement of various stent types, *Am. J. Cardiol.* **87** (2001), 34–39.
[19] A. Kastrati, J. Mehilli, J. Dirschinger et al., Intracoronary stenting and angiographic results: strut thickness effect on restenosis outcome (ISAR-STEREO) trial, *Circulation* **103** (2001), 2816–2821.
[20] C. Kleinstreuer, S. Hyun, J.R. Buchanan et al., Hemodynamic parameters and early intimal thickening in branching blood vessels, *Crit. Rev. Biomed. Eng.* **29** (2001), 1–64.
[21] D.N. Ku, D.P. Giddens, C.K. Zarins et al., Pulsatile flow and atherosclerosis in the human carotid bifurcation. Positive correlation between plaque location and low oscillating shear stress, *Arteriosclerosis* **5** (1985), 293–302.
[22] S.M. Kute and D.A. Vorp, The effect of proximal artery flow on the hemodynamics at the distal anastomosis of a vascular bypass graft: computational study, *J. Biomech. Eng.* **123** (2001), 277–283.
[23] J.F. LaDisa, I. Guler, L.E. Olson et al., Three-dimensional computational fluid dynamics modeling of alterations in coronary wall shear stress produced by stent implantation, *Ann. Biomed. Eng.* **31** (2003), 972–980.
[24] J.F. LaDisa, L.E. Olson, I. Guler et al., Stent design properties and deployment ratio influence indexes of wall shear stress: a three-dimensional computational fluid dynamics investigation within a normal artery, *J. Appl. Physiol.* **97** (2004), 424–430.
[25] J.F. LaDisa, L.E. Olson, I. Guler et al., Circumferential vascular deformation after stent implantation alters wall shear stress evaluated with time-dependent 3D computational fluid dynamics models, *J. Appl. Physiol.* **98** (2005), 947–957.
[26] J.F. LaDisa, L.E. Olson, D. Hettrick et al., Axial stent strut angle influences wall shear stress after stent implantation: analysis using 3D computational fluid dynamics models of stent foreshortening, *Biomed. Eng. Online* **4** (2005), 59.
[27] J.F. LaDisa, L.E. Olson, R.C. Molthen et al., Alterations in wall shear stress predict sites of neointimal hyperplasia after stent implantation in rabbit iliac arteries, *Am. J. Physiol. Heart Circ. Physiol.* **288** (2005), H2465–H2475.
[28] A.J. Lansky, G.S. Roubin, C.D. O'Shaughnessy et al., Randomized comparison of GR-II stent and Palmaz–Schatz stent for elective treatment of coronary stenoses, *Circulation* **102** (2000), 1364–1368.
[29] M. Lei, C. Kleinstreuer and G.A. Truskey, A focal stress gradient-dependent mass transfer mechanism for atherogenesis in branching arteries, *Med. Eng. Phys.* **18** (1996), 326–332.

[30] P.W. Longest and C. Kleinstreuer, Computational haemodynamics analysis and comparison study of arterio-venous grafts, *J. Med. Eng. Technol.* **24** (2000), 102–110.
[31] A.M. Malek, S.L. Alper and S. Izumo, Hemodynamic shear stress and its role in atherosclerosis, *JAMA* **282** (1999), 2035–2042.
[32] J. Murphy and F. Boyle, Assessment of the effects of increasing levels of physiological realism in the computational fluid dynamics analyses of implanted coronary stents, in: *Proceedings of the Engineering in Medicine and Biology Society, 30th Annual International Conference of the IEEE*, Vancouver, 2008, pp. 5906–5909.
[33] W.W. Nichols and M.F. O'Rourke, *McDonald's Blood Flow in Arteries*, Arnold, London, 1998, pp. 17–18.
[34] M. Ojha, Spatial and temporal variations of wall shear stress within an end-to-side arterial anastomosis model, *J. Biomech.* **26** (1993), 1377–1388.
[35] J.U. Pache, A. Kastrati, J. Mehilli et al., Intracoronary stenting and angiographic results: strut thickness effect on restenosis outcome (ISAR-STEREO-2) trial, *J. Am. Coll. Cardiol.* **41** (2003), 1283–1288.
[36] P.J. Prendergast, C. Lally, S. Daly et al., Analysis of prolapse in cardiovascular stents: a constitutive equation for vascular tissue and finite-element modelling, *J. Biomech. Eng.* **125** (2003), 692–699.
[37] C. Rogers and E.R. Edelman, Endovascular stent design dictates experimental restenosis and thrombosis, *Circulation* **91** (1995), 2995–3001.
[38] R. Schwartz and D.R. Holmes, Pigs, dogs, baboons, and man: lessons for stenting from animal studies, *J. Interv. Cardiol.* **7** (1994), 355–368.
[39] T. Seo, L.G. Schachter and A.I. Barakat, Computational study of fluid mechanical disturbance induced by endovascular stents, *Ann. Biomed. Eng.* **33** (2005), 444–456.
[40] S.S. White, C.K. Zarins, D.P. Giddens et al., Hemodynamic patterns in two models of end-to-side vascular graft anastomoses: effects of pulsatility, flow division, Reynolds number, and hood length, *J. Biomech. Eng.* **115** (1993), 104–111.
[41] C.K. Zarins, D.P. Giddens, B.K. Bharadvaj et al., Carotid bifurcation atherosclerosis. Quantitative correlation of plaque localization with flow velocity profiles and wall shear stress, *Circ. Res.* **53** (1983), 502–514.